Available online at www.sciencedirect.com

ScienceDirect

Procedia CIRP 138 (2026) 198–203

www.elsevier.com/locate/procedia

18th CIRP Conference on Intelligent Computation in Manufacturing Engineering

Spindle performance monitoring via accelerometer measurements in data-driven models

Gregory W. Vogl[a,*], M. Wahidur Rahman[b], and Yongzhi Qu[b]

[a]*Engineering Laboratory, National Institute of Standards and Technology (NIST), 100 Bureau Drive, Gaithersburg, Maryland 20899-8220, USA*
(Official contribution of the National Institute of Standards and Technology; not subject to copyright in the United States.)
[b]*Department of Mechanical Engineering, The University of Utah, Salt Lake City, UT 84112, USA*

* Corresponding author. Tel.: +01-301-975-3198 ; Fax: +01-301-975-8058. *E-mail address:* gvogl@nist.gov

Abstract

The future of manufacturing depends on transitioning traditional machines into intelligent machine tools that can monitor and control themselves. As the spindle is an essential component of machine tools, the performance of machine tool spindles should be tracked for quality control. For example, smart spindles could be equipped with accelerometers for monitoring the spindle performance via models that relate the measured accelerations to the spindle error motions. Various data-driven models were created that estimate spindle-related displacements from on-machine accelerations. The estimated displacements were compared, revealing the advantages and disadvantages of each model to monitor the spindle performance.

Peer-review under responsibility of the scientific committee of the 18th CIRP Conference on Intelligent Computation in Manufacturing Engineering (CIRP ICME ‘24)

Keywords: Smart manufacturing; Industry 4.0; Data-driven dynamics; Frequency response function; Machine tool; Modeling; Dynamics; Machining processes; Sensing; Monitoring; Diagnostics; Machine learning; Artificial intelligence

1. Introduction

The spindle is a vital component of modern machine tools [1]. Hence, the condition and performance of machine tool spindles should be tracked for the purposes of machine health monitoring and quality control of machined parts. The spindle error motions [2] that characterize the spindle performance change due to operational usage, e.g., with bearing defects accounting for about 40 percent of spindle damage [3]. However, methods for monitoring the spindle performance [4] typically require the use of relatively expensive metrology equipment and prohibitive setup time, which means that these methods are usually not utilized. Because the performance of spindles is typically unknown, manufacturers usually react to spindle issues, instead of being proactive to prevent or mitigate them. Therefore, the spindle error motions should be monitored by smart spindles within intelligent machine tools that can monitor and potentially control themselves. Smart spindles should assess their state of degradation as actionable intelligence for maintenance planning and the avoidance of spindle failure. Cao et al. [5] reviewed the progress of intelligent spindles and could not find one in industry that met the needs of monitoring and control of tool condition, chatter, spindle collision, temperature/thermal error, spindle balance, and spindle health.

The first step towards this future of manufacturing requires on-machine measurements. Various approaches have been created to measure on-machine spindle-related displacements. Kim et al. [6] developed a magnetic exciter with capacitive displacement sensors to magnetically apply forces and capacitively measure the translational displacements of a master bar rotating within a spindle. Matsubara et al. [7] used

2212-8271
Peer-review under responsibility of the scientific committee of the 18th CIRP Conference on Intelligent Computation in Manufacturing Engineering (CIRP ICME ‘24)
10.1016/j.procir.2026.01.035

a magnetic excitation method and spindle displacement sensor to investigate the dynamic stiffness and chatter conditions of a rotating spindle, confirming the sensitivity of the spindle stiffness to both spindle speed and temperature. Stepan et al. [8] presented a setup in which two laser beams graze the workpiece, which influences the beam intensity measured by two photodiodes for displacement measurements. Bediz et al. [9] developed a system to excite the spindle dynamics up to 20 kHz, via impact testing during rotation, while controlling the impact force and measuring the resulting radial motions of the spindle with fiber-optic laser Doppler vibrometers. Results showed that the spindle speed has a significant effect on the dynamic response of ultra-high-speed spindles [9].

In contrast to direct measurements of spindle motions, smart spindles could be equipped with accelerometers [10, 11] for indirect monitoring of the spindle performance via models that relate the measured accelerations to the spindle error motions. Accelerometers have advantages for integration into smart spindles, including their small size, cost-effectiveness, reliable signal transmission, long operational life, and simple maintenance. This paper compares different classes of data-driven models that estimate spindle-related displacements from on-machine accelerations. The first method is a physics-inspired data-driven approach [12] and the second and third methods use pure data-driven machine learning.

2. Experimental setup

The data utilized for the models comes from a custom metrology suite [13] that collects simultaneous laser displacements, on-machine accelerations, and simulated cutting forces for any spindle speed. Fig. 1 illustrates the metrology suite for data collection on a vertical machining center (VMC). Fig. 1a shows that an instrumented tool holder with a hidden magnet and an embedded laser diode is placed within the machine tool spindle. During rotation, the rotating magnet of the tool holder interacts with stationary magnets on force-torque sensors in the metrology suite, causing magnetic forces that simulate cutting. The radial and axial separations of the magnets may be changed via linear actuators and the spindle position, respectively, to change the magnetic forces. As the tool holder rotates, the accelerometers attached to the spindle housing measure vibrations. Simultaneously, as seen in Fig. 1b, a laser beam emitted from the laser diode in the instrumented tool holder is bent, split into two beams of lengths L_1 and L_2, and projected onto 10 mm × 10 mm sensors within laser position modules (LPMs) in the metrology suite. Each LPM measures the relative planar positions of the power centroid of the projected laser spot. For the given setup, L_1 and L_2 are about 0.212 m and 0.474 m, respectively. After removal of the least-squares circle [2], the four tool-to-workpiece spindle error motions are defined as

$$E_{XC} = -\alpha x_1 + (1-\alpha)x_2 \quad (1a)$$
$$E_{YC} = \alpha y_1 + (1-\alpha)y_2 \quad (1b)$$
$$E_{AC} = (y_2 - y_1)\,\alpha/L_2 \quad (1c)$$
$$E_{BC} = -(x_1 + x_2)\,\alpha/L_2 \quad (1d)$$

where the nondimensional ratio $\alpha = L_2/(L_2 - L_1)$.

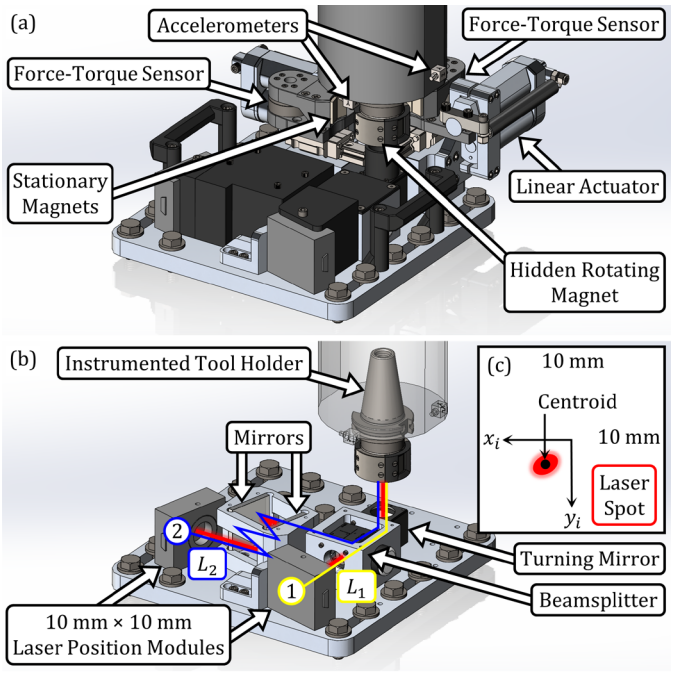

Fig. 1. Illustrations of (a) metrology suite within vertical machine tool, (b) optical components (without covers) for measurement of spindle error motions based on beam lengths, L_1 and L_2, and (c) laser spot power centroid on ith laser position module sensor.

Fig. 2 shows the experimental setup on a VMC. Two triaxial accelerometers (100 mV/g) were superglued to the spindle housing. During rotation, the magnet within the tool holder interacts with stationary magnets on the force-torque sensors (ATI Industrial Automation Mini45) in the metrology suite, causing magnetic forces ("simulated cutting forces"). The resulting forces, vibrations, and laser displacements are measured by the data acquisition (DAQ) box.

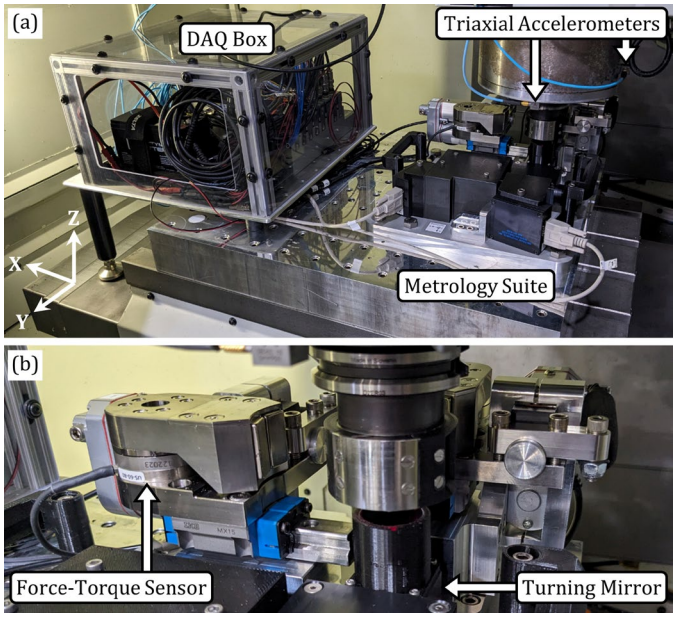

Fig. 2. (a) Metrology suite, triaxial accelerometers, and DAQ box on VMC, and (b) close-up view of instrumented tool holder with metrology suite.

A dataset was collected for various spindle speeds and forces. For a given configuration of magnets, the spindle

speed was increased from 500 r/min to 7500 r/min in a stepwise manner with an increment of 40 r/min over a period of about 9 min. At each speed, the DAQ box collects data at 25.6 kHz for 1 s. This process is repeated for each configuration of magnets, created by changing the radial positions of the stationary magnets via the linear actuators (see Fig. 1a) and/or the axial position of the rotating magnet via the machine tool Z-axis. The lowest force range was about 1 N, while the highest force range was about 200 N. The variety of forces, and hence the variety of spindle displacements, should aid the models that relate displacements and accelerations. In total, 1584 (= 176 × 9) combinations of spindle speeds and force configurations were collected. Table 1 shows the relative qualitative force ranges for the nine utilized magnet configurations.

Table 1. Relative qualitative force ranges for each configuration of magnets.

	Relative Qualitative Force Range		
Configuration Number	X-axis	Y-axis	Z-axis
1	Low	Low	Low
2	Medium	Low	Low
3	High	Low	Low
4	Low	Medium	Low
5	Low	High	Low
6	Medium	Low	Medium
7	High	Low	Medium
8	Low	Medium	Medium
9	Low	High	Medium

3. Models for displacement estimation from accelerations

Two different types of approaches were used to model the dependence of the four laser displacements described in Eq. (1) on the accelerations collected from one triaxial accelerometer. The first approach is to create a physics-inspired (PI) data-driven model while the second and third approaches are developed using machine learning (ML) models. The models are described in this section and then their performances are compared in the subsequent sections.

The PI method estimates any laser displacement, $E_i(t)$, to the on-machine vibration displacements, $x_j(t)$, as

$$\begin{aligned}\mathcal{F}(E_i) = [&H_i(CPR) + \Omega G_i(CPR) \\ &+ \Omega^2 N_i(CPR)]e^{-\mathbb{i}\theta_i(CPR)} \\ &+ \sum_{j=\mathrm{X,Y,Z}} \left[H_{ij}(f)\mathcal{F}(x_j)\right. \\ &\left.+ \Omega G_{ij}(f)\mathcal{F}(\dot{x}_j) + \Omega^2 N_{ij}(f)\mathcal{F}(x_j)\right]\end{aligned} \quad (2)$$

where t is time, f is temporal frequency, $CPR = f/f_1$ is cycles per revolution (CPR) with f_1 as the spindle speed in Hz, Ω is the spindle speed in rad/s, $\mathcal{F}$ is the Fourier transform operator, i represents sampled data for one of the four laser displacements, j is any of the three axis directions (X, Y, or Z), x_j is x, y, or z; that is, the measured vibration displacement in the jth direction, an overdot ($\dot{}$) represents differentiation with respect to time, $\mathbb{i} = \sqrt{-1}$, θ_i is the phase of $E_i(t)$ relative to a fixed rotational position of the spindle, H_i, G_i, and N_i are frequency response functions (FRFs) as functions of CPR, and H_{ij}, G_{ij}, and N_{ij} are FRFs as functions of f. As seen in Eq. (2), the PI model accounts for up to quadratic dependencies on spindle speed, like for previous models that modeled force based on accelerations [12, 13].

However, to model laser displacement based on accelerations, three additional FRFs (H_i, G_i, and N_i) were added to Eq. (2) to account for the misalignment of the laser beam to the spindle axis (at CPR = 1) and synchronous spindle error motions (at CPR = 2, 3, etc.). These terms allow for Eq. (2) to estimate the as-measured laser displacement, $E_i(t)$, without the removal of the least-squares circle. Hence, Eq. (2) models the laser misalignment and synchronous spindle error motions (the first three terms) as well as the influence of on-machine accelerations (the remaining terms) on the as-measured laser displacements described in Eq. (1) without the removal of the least-squares circle. Note that the second and third FRFs (G_i and N_i) in Eq. (2) account for changes with spindle speed, Ω, due to internal spindle forces, while the acceleration-related terms in Eq. (2) should account for the influence of external forces, e.g., cutting forces.

Equation (1) is then approximated in a similar manner to a previous approach [12], in which a linear system of equations is created and solved via the least-squares method. Each signal is fitted with harmonics up to 500 Hz and those coefficients are used to create the equations that depend on FRF values at CPRs of 1, 2, 3, …, 35 or FRF values at frequencies with varied spacings between 2 Hz and 6 Hz. The maximum CPR of 35 and the variable frequency spacing were created to help to prevent overfitting (too few data per model variable) by having each FRF variable utilized within at least 50 equations. Then, the system of equations is solved via a least-squares fit to create a model for the given laser displacement with the approximated FRFs. However, to create a model that is potentially more accurate for prediction purposes, 500 models were created with random samplings of 90 % of the simulated cutting data. These models have different FRFs due to their different data combinations used for the least-squares solution. Then, the 10 percent of the models (50 models) having the lowest root mean square error (RMSE) metric values (see Sec. 4) were averaged to create a final model for the given laser displacement, $E_i(t)$.

Two ML methods were used to develop and test models for the simulated cutting dataset described in Sec. 2. The first ML method uses XGBoost (XGB) regression [14] to create each individual model that predicts a laser displacement, $E_i(t)$. Each XGB model has the same configuration with 100 estimators, a maximum depth of six (6), and a learning rate of 0.1. Each model was trained with various features (inputs) and labels (outputs). The model inputs are composed of 10 features: (1-6) the real and imaginary parts of the harmonic components of the triaxial on-machine accelerations (up to 600 Hz for the ML models), (7) the temporal frequency (f) associated with each harmonic component, (8) the spindle speed (Ω), and (9-10) the cosine and sine of the phase (θ_i) of $E_i(t)$. The model outputs are the real and imaginary parts of the harmonic components of the given laser displacement, $E_i(t)$. This selection of features and labels aims to capture the machine's operating conditions and dynamics, enabling the models to effectively learn the relationships between operating conditions and resultant displacements.

To further investigate the performance of data-driven approaches, deep neural networks (DNNs) were also developed. The DNN architecture includes four layers with two hidden layers of 64 neurons each. Also, the inputs and outputs for the DNN models are the same as those for the XGB models, and 90 % of the data was used for training and 10 % was used for testing to avoid overfitting for these models. Previously, a data-driven regression method with a learned nonlinear basis [15] estimated the simulated cutting forces with a relatively high accuracy, so the potential exists to estimate the laser displacements with ML approaches.

All data-driven models output laser displacements with frequencies up to 500 Hz but not down to 0 Hz because integrated electronics piezoelectric (IEPE) accelerometers do not measure down to 0 Hz. Therefore, the steady-state terms in the signals were removed, so that only the periodic terms were utilized.

4. Metrics for comparison

Each model outputs one of four displacements, whether one of the two radial translational displacements or one the two tip-tilt angular displacements of the laser diode. Hence, the training performances of the models can be determined via the use of various metrics that compare the measured and modeled displacements. The metrics depend upon the displacement deviation, δ_{ij}, which is the difference between the modeled and measured displacements; that is,

$$\delta_{ij} = \hat{E}_{ij} - E_{ij} \tag{3}$$

where $\hat{E}_{ij}$ and E_{ij} are the j^{th} data points in the i^{th} modeled and measured displacement signals, respectively.

Three metrics for the i^{th} comparison are the mean absolute error (MAE_i), the root mean square error (RMSE_i), and the maximum absolute error (MaxAE_i), defined as

$$\text{MAE}_i = \frac{1}{m_i}\sum_{j=1}^{m_i}\left|\delta_{ij}\right| \tag{4}$$

$$\text{RMSE}_i = \sqrt{\frac{1}{m_i}\sum_{j=1}^{m_i}\delta_{ij}^2} \tag{5}$$

$$\text{MaxAE}_i = \max\left(\left|\delta_{ij}\right| \forall\, j\right) \tag{6}$$

where m_i is the number of data points in each i^{th} displacement signal. Equations (4)-(6) yield three populations of metric values, each having a length of $n = 1584$ because there are 1584 data files based on the unique combinations of the spindle speed and the magnetic forces. Also, the mean range (M-R) for any measured displacement signal is defined as

$$\text{M-R} = \frac{1}{n}\sum_{i=1}^{n}\left[\max\left(E_{ij} \forall\, j\right) - \min\left(E_{ij} \forall\, j\right)\right] \tag{7}$$

Thus, each model results in populations of the error metrics (MAE, RMSE, MaxAE) that are statistically analyzed in the next section to understand each model's performance.

5. Comparison of model prediction performance metrics

Table 2 shows the prediction performance metrics of the models for the four displacements based on use of the simulated cutting (magnetic force) dataset. The overall error metrics in Table 2 have the form of "mean ± standard deviation," based on the error metric populations defined in Eqs. (4)-(6) for the models applied to all displacement signals. According to Table 2, three of the PI models estimate E_{YC}, E_{AC}, and E_{BC} with average MAEs to within roughly 1 % of the respective mean ranges, while the PI model for E_{XC} has a relative average MAE of about 3 %. On the other hand, the DNN and XGB models have average MAEs that are within about 2 % to 4 % of the respective M-Rs. Therefore, the PI models are roughly twice as accurate, on average, compared to the pure ML models. Furthermore, the ratios of the standard deviations to the means of the ML-based error metric populations (whether for the MAE, RMSE, or MaxAE) are larger than those for the PI-based error metric populations. This means that the PI models have lower relative variances compared to the ML models, which is another aspect of the better prediction performance for the PI models. Finally, while the prediction errors for the DNN and XGB models are similar, the average errors of the DNNs are generally slightly higher than those of the XGB models, which means that the XGB models have slightly better average prediction performances compared to the DNN models.

While validation metrics are not shown here for the 10 % of data used for testing of all the data-driven models, the validation error metrics were similar to the prediction metrics seen in Table 2, which helps validate that overfitting was generally avoided for all the PI and ML models.

Table 2. Prediction performance metrics for the PI and ML models for the VMC with the simulated cutting dataset. The metrics have the form of "mean ± standard deviation."

		Metric			
Disp.	Model	MAE	RMSE	MaxAE	M-R
E_{XC} (μm)	PI	5.40 ± 2.07	6.26 ± 2.32	11.4 ± 4.00	162
	DNN	8.14 ± 3.46	9.66 ± 4.03	19.4 ± 8.23	
	XGB	6.69 ± 3.79	8.00 ± 4.40	16.1 ± 8.38	
E_{YC} (μm)	PI	1.69 ± 0.649	2.02 ± 0.778	4.04 ± 1.57	198
	DNN	5.85 ± 3.75	7.10 ± 4.60	15.0 ± 9.76	
	XGB	6.28 ± 4.82	7.61 ± 5.64	16.0 ± 11.4	
E_{AC} (μrad)	PI	32.4 ± 16.8	36.4 ± 18.6	57.2 ± 27.1	3270
	DNN	73.7 ± 49.5	86.1 ± 59.6	162 ± 118	
	XGB	61.2 ± 93.0	71.3 ± 105	132 ± 181	
E_{BC} (μrad)	PI	32.2 ± 16.3	36.5 ± 17.8	60.6 ± 26.2	3300
	DNN	89.3 ± 62.6	106 ± 77.0	210 ± 153	
	XGB	77.6 ± 79.3	91.1 ± 94.3	174 ± 194	

Fig. 3 compares the ranges of the four modeled and measured displacements for the PI models in Fig. 3(a,b), the DNNs in Fig. 3(c,d), and the XGB models in Fig. 3(e,f). As seen in the metrics listed in Table 2, the models are not perfect, which is why the plot markers do not generally

coincide with the dashed identity lines. Even though the PI-based metrics have mean absolute errors around 2 % of the ranges, the modeled ranges in Fig. 3(a,b) have significantly larger outliers with relative errors of up to about 25 %. Nonetheless, the PI-modeled ranges nominally match the measured ranges, which is needed for process monitoring purposes.

In contrast, the other data-driven models have significantly larger variances in their predicted ranges, as seen in Fig. 3(c-f), compared to those for the PI models. Also, the DNNs produce fewer outliers in the predicted ranges in Fig. 3(c-d) compared to those for the XGB models in Fig. 3(e-f), which is consistent with the metrics in Table 2. The standard deviations for the XGB models for E_{XC} and E_{YC} are roughly 15 % larger than those for the DNNs, while the the standard deviations for the XGB models for E_{AC} and E_{BC} are between about 25 % and 100 % larger than those for the DNNs. These differences in variances are reflected in Fig. 3.

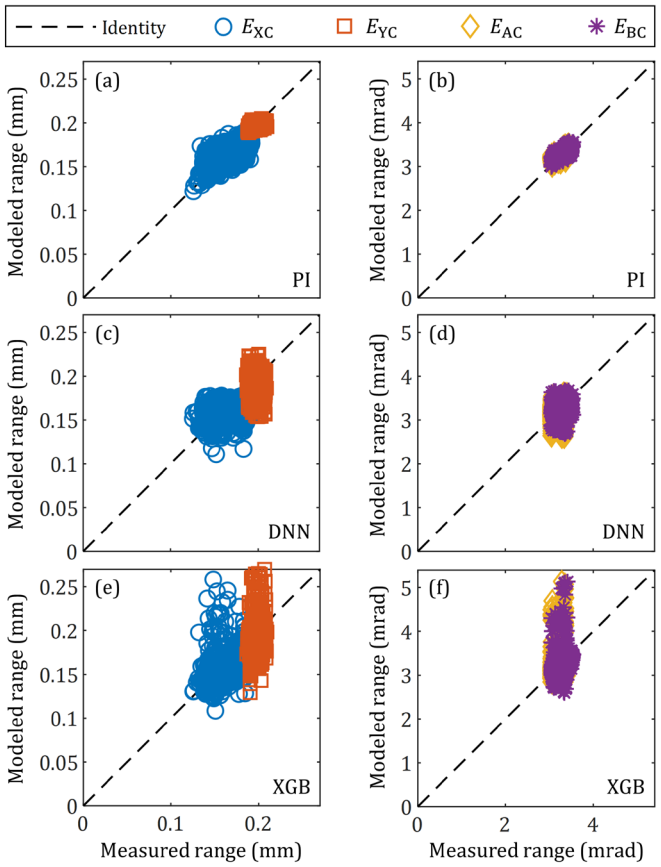

Fig. 3. Modeled displacement range versus the measured displacement range for all simulated cutting tests, using the PI models for (a) E_{XC} and E_{YC} and (b) E_{AC} and E_{BC}, the NN models for (c) E_{XC} and E_{YC} and (d) E_{AC} and E_{BC}, and the XGB models for (e) E_{XC} and E_{YC} and (f) E_{AC} and E_{BC}.

6. Investigation of spindle performance

The models can now be used to investigate the spindle performance. As previously noted, the PI model for each laser displacement contains CPR-related FRFs (H_i, G_i, and N_i) to account for the misalignment of the laser beam to the spindle axis (at $CPR = 1$) and synchronous spindle error motions (at $CPR = 2, 3$, etc.). Fig. 4 shows the modeled laser displacements (E_{XC}, E_{YC}, E_{AC}, and E_{BC}) using only the CPR-related FRFs. Hence, Fig. 4 represents the modeled laser misalignment coupled with the synchronous spindle error motions as functions of the spindle speed from 0 r/min to 7500 r/min. As seen in Fig. 4, a radial misalignment of roughly 100 µm and a tilt misalignment of about 1.6 mrad exist for the laser when the spindle is stationary (0 r/min).

Also, the laser displacements change significantly as the spindle speed increases. The trajectories deviate from their approximately circular shapes, perhaps due to speed-dependent changes in internal spindle forces. Ideally, these deviations relate to changes in the spindle performance. However, one source of measurement uncertainty is the frequency response of the laser diode, which should be characterized to understand its bandwidth for measurement purposes. Additional sources of measurement uncertainty include the laser position modules and the optics within the metrology suite, which may exhibit potential nonlinearities, as well as air currents and other environmental influences. Hence, the calibration of the laser position modules should be improved and any laser-based spindle motions should be verified with an internationally accepted standard method [2].

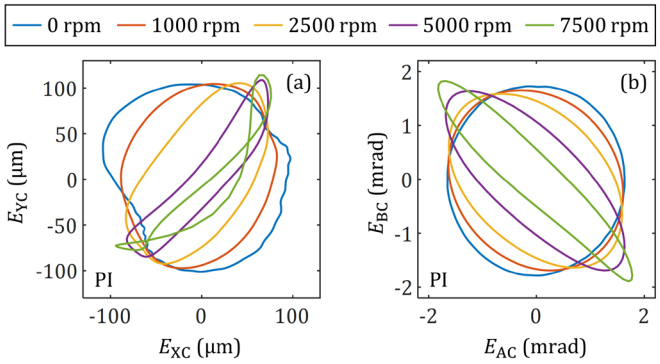

Fig. 4. Modeled laser displacements (a) E_{XC} and E_{YC} and (b) E_{AC} and E_{BC} using only CPR-related FRFs (H_i, G_i, and N_i). All responses are filtered to remove terms with frequencies > 500 Hz, since those terms are not modeled.

7. Comparison of model predictions

Fig. 5 compares the measured, PI-modeled, and XGB-modeled laser displacements for spindle speeds from 500 r/min to 5500 r/min under two different magnetic forcing conditions per spindle speed: the case with the lowest X-, Y-, and Z-axis magnetic force range (< 10 N) and the case with the highest X-axis magnetic force range (> 140 N). As expected from the metrics in Table 2, the PI models are shown in Fig. 5 to generally outperform the XGB models in modeling the displacements to match the measured trajectories. Nonetheless, all the models are nominally able to model how spindle speeds and forces (via accelerations) affect the laser displacements. Also, the ML models have the potential for improved prediction capabilities. Note that each PI model has 2211 trainable FRF parameters, while both ML models are much larger with 4994 trainable parameters for each DNN and up to 12700 nodes for each XGB model. Despite the additional complexity, the DNN and XGB models did not outperform the PI models, perhaps due to the need for a larger amount of training data for the ML models.

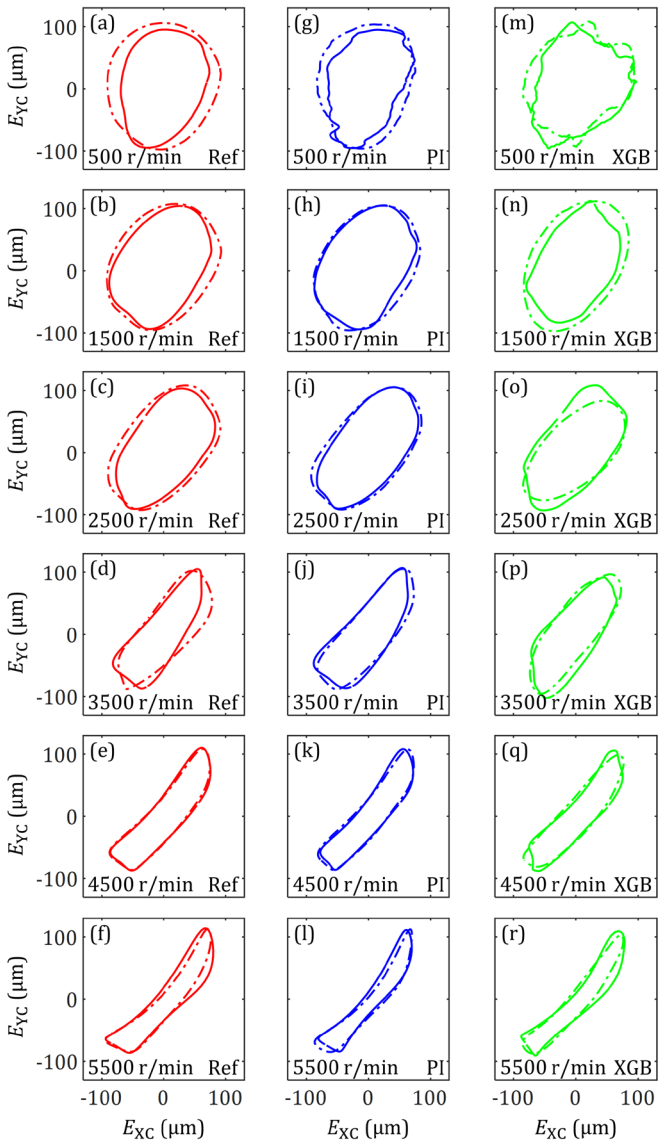

Fig. 5. (a-f) Measured, (g-l) PI-modeled, and (m-r) XGB-modeled laser displacements, E_{XC} and E_{YC}, for spindle speeds from 500 r/min to 5500 r/min. At each speed, the responses for two different cases are compared: dash-dotted curves are for the case with the lowest X-, Y-, and Z-axis magnetic force ranges (< 10 N), while solid curves are for the case with the highest X-axis magnetic force range (> 140 N).

8. Conclusions

Various data-driven models (physics-inspired models, deep neural network models, and XGBoost models) were developed to estimate the laser diode displacements of an instrumented tool holder from on-machine accelerations using training data collected from a metrology suite while the tool holder encounters simulated (magnetic) cutting forces. The physics-inspired models estimate the two translational and two angular displacements with mean absolute errors (MAEs) of about 2 % of the mean displacement ranges, which was generally better than the performance of the machine learning models with relative average MAEs of roughly 4 %. Nonetheless, all methods show the potential for monitoring real-time spindle-related displacements via on-machine accelerations, for the optimization of parts production.

Acknowledgements

The authors thank the Fabrication Technology Office at NIST for their significant contributions towards the experimental setup.

NIST disclaimer

Certain commercial equipment, instruments, or materials are identified in this paper in order to specify the experimental procedure adequately. Such identification is not intended to imply recommendation or endorsement by NIST, nor is it intended to imply that the materials or equipment identified are necessarily the best available for the purpose. This material is declared a work of the U.S. Government and is not subject to copyright protection in the United States. Approved for public release; distribution is unlimited.

References

[1] Abele E, Altintas Y, Brecher C (2010) Machine Tool Spindle Units. *CIRP Annals - Manuf Technol* 59(2):781-802.
[2] International Organization for Standardization (ISO). ISO 230-7 - Test Code for Machine Tools − Part 7: Geometric Accuracy of Axes of Rotation. 2015.
[3] Abele E, Dervisopoulos M, Kreis M (2006) Beeinflussbarkeit Von Lebenszykluskosten Durch Wissensaustausch—Produzieren Mit Blick Auf Die Lebenszykluskosten. *wt Werkstatttechnik online* 96:447-454.
[4] Gao W, Ibaraki S, Donmez MA, Kono D, Mayer JRR, Chen Y-L, et al. (2023) Machine Tool Calibration: Measurement, Modeling, and Compensation of Machine Tool Errors. *Int J Mach Tools Manuf* 187:104017.
[5] Cao HR, Zhang XW, Chen XF (2017) The Concept and Progress of Intelligent Spindles: A Review. *Int J Mach Tools Manuf* 112:21-52.
[6] Kim J, Chang H, Han D, Jang D, Oh S (2005) Cutting Force Estimation by Measuring Spindle Displacement in Milling Process. *CIRP Annals - Manuf Technol* 54(1):67-70.
[7] Matsubara A, Tsujimoto S, Kono D (2015) Evaluation of Dynamic Stiffness of Machine Tool Spindle by Non-Contact Excitation Tests. *CIRP Annals - Manuf Technol* 64(1):365-368.
[8] Stepan G, Beri B, Miklos A, Wohlfart R, Bachrathy D, Porempovics G, et al. (2019) On Stability of Emulated Turning Processes in HIL Environment. *CIRP Annals - Manuf Technol* 68(1):405-408.
[9] Bediz B, Gozen BA, Korkmaz E, Ozdoganlar OB (2014) Dynamics of Ultra-High-Speed (UHS) Spindles Used for Micromachining. *Int J Mach Tools Manuf* 87:27-38.
[10] Postel M, Aslan D, Wegener K, Altintas Y (2019) Monitoring of Vibrations and Cutting Forces with Spindle Mounted Vibration Sensors. *CIRP Annals - Manuf Technol* 68(1):413-416.
[11] Liu Y-P, Altintas Y (2021) In-Process Identification of Machine Tool Dynamics. *CIRP J Manuf Sci Technol* 32:322-337.
[12] Vogl GW, Qu Y, Eischens R, Corson G, Schmitz T, Honeycutt A, et al. Cutting Force Estimation from Machine Learning and Physics-Inspired Data-Driven Models Utilizing Accelerometer Measurements. 17th CIRP Conference on Intelligent Computation in Manufacturing Engineering (CIRP ICME). Gulf of Naples, IT: Procedia CIRP; 2023.
[13] Vogl GW, Regli DA, Corson GM (2022) Real-Time Estimation of Cutting Forces Via Physics-Inspired Data-Driven Model. *CIRP Annals - Manuf Technol* 71(1):317-320.
[14] Chen T, Guestrin C. XGBoost: A Scalable Tree Boosting System. 22nd ACM SIGKDD International Conference on Knowledge Discovery and Data Mining: ACM; 2016. pp. 785-794.
[15] Fabro J, Vogl GW, Qu Y (2022) Run-Time Cutting Force Estimation Based on Learned Nonlinear Frequency Response Function. *J Manuf Sci Eng* 144(9)